J. Fluid Mech. (2010), *vol.* 649, *pp.* 115–134. © Cambridge University Press 2010
doi:10.1017/S0022112009993259

Linear stability of Hunt's flow

JĀNIS PRIEDE†, SVETLANA ALEKSANDROVA AND SERGEI MOLOKOV

Applied Mathematics Research Centre, Department of Mathematical Sciences, Coventry University, Priory Street, Coventry CV1 5FB, UK

(Received 13 February 2009; revised 29 October 2009; accepted 2 November 2009)

We analyse numerically the linear stability of the fully developed flow of a liquid metal in a square duct subject to a transverse magnetic field. The walls of the duct perpendicular to the magnetic field are perfectly conducting whereas the parallel ones are insulating. In a sufficiently strong magnetic field, the flow consists of two jets at the insulating walls and a near-stagnant core. We use a vector stream function formulation and Chebyshev collocation method to solve the eigenvalue problem for small-amplitude perturbations. Due to the two-fold reflection symmetry of the base flow the disturbances with four different parity combinations over the duct cross-section decouple from each other. Magnetic field renders the flow in a square duct linearly unstable at the Hartmann number $Ha \approx 5.7$ with respect to a disturbance whose vorticity component along the magnetic field is even across the field and odd along it. For this mode, the minimum of the critical Reynolds number $Re_c \approx 2018$, based on the maximal velocity, is attained at $Ha \approx 10$. Further increase of the magnetic field stabilizes this mode with Re_c growing approximately as Ha. For $Ha > 40$, the spanwise parity of the most dangerous disturbance reverses across the magnetic field. At $Ha \approx 46$ a new pair of most dangerous disturbances appears with the parity along the magnetic field being opposite to that of the previous two modes. The critical Reynolds number, which is very close for both of these modes, attains a minimum, $Re_c \approx 1130$, at $Ha \approx 70$ and increases as $Re_c \approx 91 Ha^{1/2}$ for $Ha \gg 1$. The asymptotics of the critical wavenumber is $k_c \approx 0.525 Ha^{1/2}$ while the critical phase velocity approaches 0.475 of the maximum jet velocity.

1. Introduction

Application of a strong magnetic field to a flow of an electrically conducting fluid is associated primarily with two effects. Firstly, the magnetic field acts on the mean flow profile often creating inflexion points (Kakutani 1964), shear layers (Lehnert 1952) and jets (Hunt 1965), thus destabilizing the otherwise stable flow. Secondly, strong magnetic field tends to damp three-dimensional perturbations making them anisotropic, aligned with the magnetic field, and to transform them into quasi-two-dimensional structures (Moffatt 1967; Davidson 1995). There are flows, which combine the effect of high electromagnetic damping in some flow regions, high transverse shear in other regions, such as jets, and moderate stretching along the magnetic field. Instabilities and turbulence may strongly affect the transfer of momentum,

† Email address for correspondence: J.Priede@coventry.ac.uk

https://doi.org/10.1017/S0022112009993259 Published online by Cambridge University Press

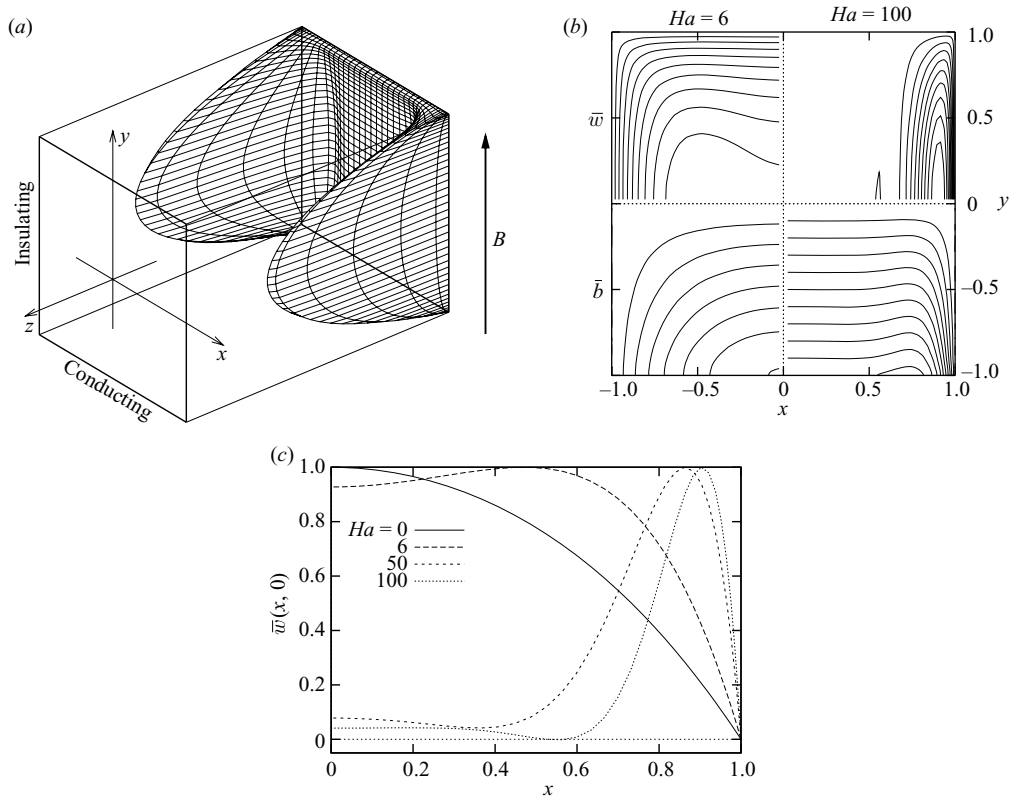


FIGURE 1. Sketch to the formulation of the problem with the base flow profile for $Ha = 100$ (a), isolines of base flow ($y > 0$) and electric current lines ($y < 0$) for $Ha = 6$ ($x < 0$) and $Ha = 100$ ($x > 0$) shown in the respective quadrants of duct cross-section (b) and the base flow velocity profiles at $y = 0$ for $Ha = 0, 6, 50, 100$ (c).

heat and mass in such liquid metal flows which are of major importance for various industrial applications ranging from metallurgy and semiconductor crystal growth (Davidson 1999) to the designs of fusion reactors with magnetic confinement (Bühler 2007).

Here we will be concerned with linear stability of the fully developed isothermal magnetohydrodynamic (MHD) flow in a constant-area square duct with a pair of perfectly electrically conducting and another pair of perfectly insulating walls in the presence of a strong magnetic field. The field is parallel to the insulating walls and perpendicular to the conducting ones, and such a flow is known as the Hunt's flow (Hunt 1965). For strong magnetic fields this flow has a pair of characteristic sidewall jets developing along the insulating walls while the velocity in the core of the duct is significantly reduced (see figure 1). These effects are due to the pattern of the electric currents, shown in figure 1(b) for $y < 0$. In the core of the duct the electric currents are induced in the direction transverse to the magnetic field and, thus, the resulting electromagnetic force nearly balances the pressure gradient driving the flow. At the insulating sidewalls, the electric current turns almost parallel to the magnetic field and, thus, the electromagnetic braking force in these regions is significantly reduced. As a result, the applied pressure gradient is balanced there

https://doi.org/10.1017/S0022112009993259 Published online by Cambridge University Press

mainly by the viscous shear, and the flow protrudes through the magnetic field in thin jets along the sidewalls. In the limit of a very strong magnetic field, the jets, which are of fundamental importance for liquid metal blankets in fusion reactors (see e.g. Molokov 1993; Molokov & Bühler 1994; Stieglitz *et al.* 1996) carry almost all of the volume flux in the so-called parallel layers. Such a velocity profile is highly unstable, as has been confirmed experimentally by Gelfgat, Dorofeev & Scherbinin (1971) and Platnieks & Freibergs (1972). Linear stability analysis of Hunt's flow has been attempted by Fujimura (1989) by assuming two-dimensional mean velocity profile and two-dimensional disturbances, both in the mid-plane of the duct transverse to the field. His results are of limited interest owing to the three-dimensional nature of both the mean profile and the disturbances. A three-dimensional linear stability analysis of a single sidewall jet has been carried out by Ting *et al.* (1991). They consider the flow in a rectangular duct with thin conducting walls in the presence of a strong transverse magnetic field. Although Ting *et al.* (1991) assume the wall conductance ratio to be small, the magnetic field is supposed to be so strong that the relative conductance of both Hartmann and parallel layers is even smaller than that of the walls. As a result, the induced electric current passes from the core region directly through the parallel layer into the sidewall to close through normal walls back to the core region. Thus, both the sidewalls and Hartmann walls are treated by Ting *et al.* (1991) as effectively well-conducting boundaries. Direct numerical simulation of this flow has been undertaken by Mück (2000) for the Reynolds number significantly above the linear stability threshold for the side layers predicted by Ting *et al.* (1991).

Here, we present the results of the three-dimensional linear stability analysis of Hunt's flow in a square duct, which according to Tatsumi & Yoshimura (1990) is linearly stable in the absence of a magnetic field. We show that the instability is far more complex than predicted by Ting *et al.* (1991) and Fujimura (1989) using asymptotic theory and two-dimensional approximation, respectively. A magnetic field of moderate strength is found to render the flow linearly unstable with respect to two pairs of antisymmetric streak-like perturbations of the axial velocity concentrated in the middle part of the duct. The most dangerous perturbation is essentially three-dimensional with the component of vorticity along the magnetic field being even and odd function across and along the magnetic field, respectively. This instability is associated with the appearance of two velocity minima in the centre of the duct which at stronger magnetic fields develop into the sidewall jets. As the magnetic field strength increases, another essentially three-dimensional instability mode with the opposite parity across the magnetic field appears. The critical wavelength of both these modes exceeds the width of the duct several times even in relatively strong magnetic fields. At the same time, the phase velocity strongly correlates with the maximum jet velocity. In a sufficiently strong magnetic field, the critical Reynolds number, based on the maximum velocity, increases nearly directly with the magnetic field strength. As the sidewall jets develop, two new, much more unstable modes appear with the parity along the magnetic field opposite to that of two previous modes. The critical Reynolds number, which is almost the same for the last two modes, increases at high magnetic fields inversely with the side layer thickness while the critical wavelength reduces directly with the thickness.

The paper is organized as follows. In § 2 we formulate the problem. Numerical method is outlined and verified in § 3 and numerical results are discussed in § 4. Section 5 summarizes and concludes the paper.

https://doi.org/10.1017/S0022112009993259 Published online by Cambridge University Press

2. Problem formulation

Consider a flow of an incompressible viscous electrically conducting liquid with density ρ, kinematic viscosity ν and electrical conductivity σ driven by a constant gradient of pressure p applied along a straight duct of rectangular cross-section with half-width d and half-height h subject to a homogeneous transverse magnetic field $\boldsymbol{B}$. The walls of the duct perpendicular to the magnetic field are perfectly conducting whereas the parallel ones are insulating.

The velocity distribution $\boldsymbol{v}$ of the flow is governed by the Navier–Stokes equation

$$\partial_t \boldsymbol{v} + (\boldsymbol{v}\cdot\nabla)\boldsymbol{v} = -\frac{1}{\rho}\nabla p + \nu\nabla^2\boldsymbol{v} + \frac{1}{\rho}\boldsymbol{f}, \tag{2.1}$$

where $\boldsymbol{f} = \boldsymbol{j}\times\boldsymbol{B}$ is the electromagnetic body force involving the induced electric current, which is governed by the Ohm's law for a moving medium

$$\boldsymbol{j} = \sigma(\boldsymbol{E} + \boldsymbol{v}\times\boldsymbol{B}), \tag{2.2}$$

where $\boldsymbol{E}$ is the electric field. The flow is assumed to be sufficiently slow so that the induced magnetic field is negligible with respect to the imposed one, implying the magnetic Reynolds number $Rm = \mu_0\sigma v_0 d \ll 1$, where μ_0 is the permeability of vacuum and v_0 is the characteristic velocity of the flow. In addition, we assume that the characteristic time of velocity variation is much longer than the magnetic diffusion time $\tau_m = \mu_0\sigma d^2$ that allows us to use the quasi-stationary approximation, according to which $\boldsymbol{E} = -\nabla\phi$, where ϕ is the electrostatic potential. The velocity and current satisfy the mass and charge conservation $\nabla\cdot\boldsymbol{v} = \nabla\cdot\boldsymbol{j} = 0$. Applying the latter to the Ohm's law (2.2) yields

$$\nabla^2\phi = \boldsymbol{B}\cdot\boldsymbol{\omega}, \tag{2.3}$$

where $\boldsymbol{\omega} = \nabla\times\boldsymbol{v}$ is vorticity. At the walls of the duct S, the normal (n) and tangential (τ) velocity components satisfy the impermeability and no-slip boundary conditions, namely $v_n|_s = 0$ and $v_\tau|_s = 0$. The conditions for the electric current at insulating and perfectly conducting walls are $j_n|_s = 0$ and $j_\tau|_s = 0$, respectively. Boundary conditions for the current and velocity applied to Ohm's law result in $\partial_n\phi|_s = 0$ and $\phi|_s = \text{const.}$ for ϕ at insulating and perfectly conducting walls, respectively.

We employ the Cartesian coordinates with the origin set at the centre of the duct and with x, y and z axes directed along the width, height and length of the duct, respectively, as shown in figure 1, with the velocity distribution given by $\boldsymbol{v} = (u, v, w)$. The problem admits a purely rectilinear base flow with a single velocity component along the duct $\bar{\boldsymbol{v}} = (0, 0, \bar{w}(x, y))$ which is shown in figure 1(a) for $Ha = 100$. In the following, all variables are non-dimensionalized by using the maximum velocity $\bar{w}_0$ and the half-width of the duct d as the velocity and length scales, while the time, pressure, magnetic field and electrostatic potential are scaled by d^2/ν, $\rho\bar{w}_0^2$, $B = |\boldsymbol{B}|$ and $\bar{w}_0 dB$, respectively. Note that we use the maximum rather than average velocity as the characteristic scale because the stability of this flow is determined by the former as discussed in the following.

Base flow can more conveniently be described using the z component of the induced magnetic field $\bar{b}$ instead of the electrostatic potential $\bar{\phi}$ (Moreau 1990). This temporal change of variables does not affect the following linear stability analysis which requires the base flow profile but not the electrostatic potential. Then the governing equations for the base flow take the form

$$\nabla^2\bar{w} + Ha\partial_y\bar{b} = \bar{P}, \tag{2.4}$$

$$\nabla^2\bar{b} + Ha\partial_y\bar{w} = 0, \tag{2.5}$$

https://doi.org/10.1017/S0022112009993259 Published online by Cambridge University Press

where $Ha = dB\sqrt{\sigma/(\rho\nu)}$ is the Hartmann number and $\bar{b}$ is scaled by $\mu_0\sqrt{\sigma\rho\nu^3}/d$. Note that the isolines of $\bar{b}$ represent electric current lines which are shown in the bottom part of figure 1(*b*) for $Ha = 6$ and $Ha = 100$. The dimensionless constant axial pressure gradient $\bar{P}$, which drives the flow, is determined from the normalization condition $\bar{w}_{max} = 1$. The velocity satisfies the no-slip boundary condition $\bar{w} = 0$ at $x = \pm 1$ and $y = \pm A$, where $A = h/d$ is the aspect ratio, which is equal to 1 for the square cross-section duct considered in this study. The boundary conditions for the induced magnetic field at insulating and perfectly conducting walls are $\bar{b} = 0$ ($x = \pm 1$) and $\partial_y \bar{b} = 0$ ($y = \pm A$), respectively. The base flow is obtained numerically by the Chebyshev collocation method which is described and validated in the next section.

In order to satisfy the incompressibility constraint $\nabla \cdot \boldsymbol{v} = 0$ for the flow perturbation, we are looking for the velocity distribution as $\boldsymbol{v} = \nabla \times \boldsymbol{\psi}$, where $\boldsymbol{\psi}$ is a vector stream function. The vector stream function, as the magnetic vector potential $\boldsymbol{A}$ in electrodynamics, is defined up to a gradient of an arbitrary function which added to $\boldsymbol{\psi}$ does not change $\boldsymbol{v}$. In order to eliminate this ambiguity, we impose an additional constraint on $\boldsymbol{\psi}$

$$\nabla \cdot \boldsymbol{\psi} = 0, \tag{2.6}$$

which is analogous to the Coulomb gauge for $\boldsymbol{A}$ (Jackson 1998). This gauge, similar to the incompressibility constraint for $\boldsymbol{v}$, leaves only two independent components of $\boldsymbol{\psi}$.

The pressure gradient is eliminated by applying *curl* to (2.1) which yields two dimensionless equations for $\boldsymbol{\psi}$ and $\boldsymbol{\omega}$

$$\partial_t \boldsymbol{\omega} = \nabla^2 \boldsymbol{\omega} - Re\boldsymbol{g} + Ha^2 \boldsymbol{h}, \tag{2.7}$$

$$0 = \nabla^2 \boldsymbol{\psi} + \boldsymbol{\omega}, \tag{2.8}$$

where $\boldsymbol{g} = \nabla \times (\boldsymbol{v} \cdot \nabla)\boldsymbol{v}$ and $\boldsymbol{h} = \nabla \times \boldsymbol{f}$ are the *curls* of the dimensionless convective inertial and electromagnetic forces, respectively, and $Re = \bar{w}_0 d/\nu$ is the Reynolds number. In fusion blanket applications $Re \sim 10^1$–10^5 while $Ha \sim 10^3$–10^4.

The boundary conditions for $\boldsymbol{\psi}$ and $\boldsymbol{\omega}$ are obtained as follows. The impermeability condition applied integrally as $\int_s \boldsymbol{v} \cdot \mathrm{d}\boldsymbol{s} = \oint_l \boldsymbol{\psi} \cdot \mathrm{d}\boldsymbol{l} = 0$ to an arbitrary area of the wall s encircled by a contour l yields $\psi_\tau|_s = 0$. Using this boundary condition, which implies $\boldsymbol{\psi}|_s = \boldsymbol{n}\psi_n|_s$, in combination with (2.6) we obtain $\partial_n \psi_n|_s = 0$. In addition, the no-slip condition applied integrally $\oint_l \boldsymbol{v} \cdot \mathrm{d}\boldsymbol{l} = \int_s \boldsymbol{\omega} \cdot \mathrm{d}\boldsymbol{s}$ yields $\omega_n|_s = 0$.

We analyse linear stability of the base flow $\{\bar{\boldsymbol{\psi}}, \bar{\boldsymbol{\omega}}, \bar{\phi}\}(x, y)$ with respect to infinitesimal disturbances in the form of harmonic waves travelling along the axis of the duct

$$\{\boldsymbol{\psi}, \boldsymbol{\omega}, \phi\}(\boldsymbol{r}, t) = \{\bar{\boldsymbol{\psi}}, \bar{\boldsymbol{\omega}}, \bar{\phi}\}(x, y) + \{\hat{\boldsymbol{\psi}}, \hat{\boldsymbol{\omega}}, \hat{\phi}\}(x, y)\mathrm{e}^{\gamma t + \mathrm{i}kz},$$

where k is a wavenumber and γ is, in general, a complex growth rate. Upon substituting the solution sought in such a form into (2.7) and (2.8), we obtain the governing equations for the disturbance amplitudes

$$\gamma \hat{\boldsymbol{\omega}} = \nabla_k^2 \hat{\boldsymbol{\omega}} - Re\hat{\boldsymbol{g}} + Ha^2 \hat{\boldsymbol{h}}, \tag{2.9}$$

$$0 = \nabla_k^2 \hat{\boldsymbol{\psi}} + \hat{\boldsymbol{\omega}}, \tag{2.10}$$

$$0 = \nabla_k^2 \hat{\phi} - \hat{\omega}_y, \tag{2.11}$$

where $\nabla_k \equiv \nabla + \mathrm{i}k\boldsymbol{e}_z$. Because of the solenoidity constraint satisfied by $\hat{\boldsymbol{\omega}}$ similarly to $\hat{\boldsymbol{\psi}}$, we need only the x and y components of (2.9), namely $\hat{h}_x = -\partial_{xy}\hat{\phi} - \partial_y \hat{w}$,

https://doi.org/10.1017/S0022112009993259 Published online by Cambridge University Press

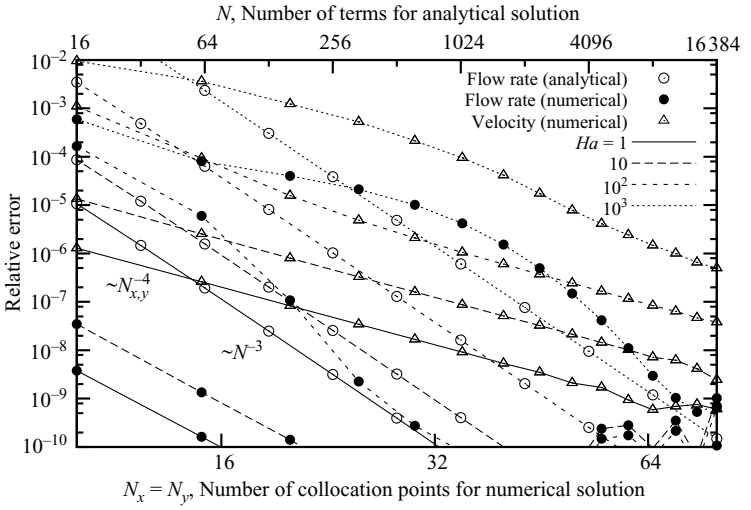


FIGURE 2. Accuracy of the base flow at various Hartmann numbers depending on the number of terms in the Fourier series solution (top axis) and the number of collocation points for numerical solution (bottom axis).

$\hat{h}_y = -\partial_{yy}\hat{\phi}$ and

$$\hat{g}_x = k^2\hat{v}\bar{w} + \partial_{yy}(\hat{v}\bar{w}) + \partial_{xy}(\hat{u}\bar{w}) + \mathrm{i}2k\partial_y(\hat{w}\bar{w}), \tag{2.12}$$

$$\hat{g}_y = -k^2\hat{u}\bar{w} - \partial_{xx}(\hat{u}\bar{w}) - \partial_{xy}(\hat{v}\bar{w}) - \mathrm{i}2k\partial_x(\hat{w}\bar{w}), \tag{2.13}$$

where $\hat{u} = \mathrm{i}k^{-1}(\partial_{yy}\hat{\psi}_y - k^2\hat{\psi}_y + \partial_{xy}\hat{\psi}_x)$, $\hat{v} = -\mathrm{i}k^{-1}(\partial_{xx}\hat{\psi}_x - k^2\hat{\psi}_x + \partial_{xy}\hat{\psi}_y)$ and $\hat{w} = \partial_x\hat{\psi}_y - \partial_y\hat{\psi}_x$. The relevant boundary conditions are

$$\partial_x\hat{\phi} = \hat{\psi}_y = \partial_x\hat{\psi}_x = \partial_x\hat{\psi}_y - \partial_y\hat{\psi}_x = \hat{\omega}_x = 0 \text{ at } x = \pm 1, \tag{2.14}$$

$$\hat{\phi} = \hat{\psi}_x = \partial_y\hat{\psi}_y = \partial_x\hat{\psi}_y - \partial_y\hat{\psi}_x = \hat{\omega}_y = 0 \text{ at } y = \pm A. \tag{2.15}$$

3. Numerical method

We solve the problem posed by (2.4)–(2.5) and (2.9)–(2.11) with the boundary conditions (2.14), (2.15) by a spectral collocation method on a Chebyshev–Lobatto grid using even number of points in the x and y directions given by $2N_x + 2$ and $2N_y + 2$, respectively, where $N_{x,y} = 30 \ldots 55$ is used depending on Ha and Re. The convergence of the numerical solution for the base flow was validated against the Fourier series solution of Hunt (1965). Firstly, we looked at the relative error in the flow rate for a fixed pressure gradient. As seen in figure 2, analytical solution for this quantity converges as $O(N^{-3})$ and requires $\approx 10^3$ terms at $Ha = 10^3$ for the relative accuracy of $\approx 10^{-6}$. The numerical solution for the flow rate shows a faster-than-algebraic convergence rate developing at sufficiently high resolution, which is typical for spectral methods. Secondly, maximum error in velocity scaled with respect to the velocity maximum for $N_x = N_y$ decreases as $O(N_{x,y}^{-4})$. For $Ha = 10^3$, the resolution of $N_x \times N_y = 50 \times 50$ ensures the relative accuracy in the base flow velocity of about 10^{-5}. The convergence of the linear stability problem, for which the resolution of the base flow is necessary but not sufficient, is tested below.

https://doi.org/10.1017/S0022112009993259 Published online by Cambridge University Press

	I	II	III	IV
$\hat{\psi}_x, \hat{\omega}_x, \hat{v}$:	(o, o)	(o, e)	(e, o)	(e, e)
$\hat{w}$:	(o, e)	(o, o)	(e, e)	(e, o)
$\hat{\psi}_z, \hat{\omega}_z$:	(e, o)	(e, e)	(o, o)	(o, e)
$\hat{\psi}_y, \hat{\omega}_y, \hat{u}, \hat{\phi}$:	(e, e)	(e, o)	(o, e)	(o, o)

TABLE 1. The (x, y) parities of different variables for symmetries I, II, III and IV; e – even, o – odd.

Because of the double reflection symmetry of the base flow with respect to $x=0$ and $y=0$ planes, small-amplitude perturbations with different parities in x and y decouple from each other. This results in four mutually independent modes which we classify as (o, o), (o, e), (e, o) and (e, e) according to whether the x and y symmetry of $\hat{\psi}_x$ is odd or even, respectively. Our classification of modes specified in table 1 corresponds to the symmetries I, II, III and IV used by Tatsumi & Yoshimura (1990) and Uhlmann & Nagata (2006). As a result, the problem is broken up into four independent problems of different symmetries defined in one quadrant of the duct cross-section with $N_x \times N_y$ internal collocation points. This allows us to reduce the size of the matrix in the eigenvalue problem, which is derived below, by a factor of 16. For each symmetry, we represent (2.9), (2.10) in the matrix form

$$\gamma \boldsymbol{\omega}_0 = \boldsymbol{A}_0 \boldsymbol{\omega}_0 + \boldsymbol{A}_1 \boldsymbol{\omega}_1 + \boldsymbol{f}_0, \tag{3.1}$$

$$0 = \boldsymbol{B}_0 \boldsymbol{\psi}_0 + \boldsymbol{\omega}_0, \tag{3.2}$$

where $\boldsymbol{\psi}_0$ and $\boldsymbol{\omega}_0$ are the values of $(\hat{\psi}_x, \hat{\psi}_y)$, $(\hat{\omega}_x, \hat{\omega}_y)$ at the internal collocation points, $\boldsymbol{\omega}_1$ are unknown values of the tangential component of $(\hat{\omega}_x, \hat{\omega}_y)$ at $N_x + N_y$ boundary points; $\boldsymbol{f}_0$ stands for the source term in (2.9), $\boldsymbol{A}_0$, $\boldsymbol{A}_1$ and $\boldsymbol{B}_0$ matrices represent collocation approximation of ∇_k^2 operator with the explicit boundary conditions (2.14), (2.15) eliminated. For the unknown boundary values of $\boldsymbol{\omega}_1$, we have an extra boundary condition $\partial_x \hat{\psi}_y - \partial_y \hat{\psi}_x = 0$ imposed on $(\hat{\psi}_x, \hat{\psi}_y)$ at $N_x + N_y$ boundary points which is represented as

$$\boldsymbol{C}_0 \boldsymbol{\psi}_0 = 0. \tag{3.3}$$

To obtain a conventional matrix eigenvalue problem for γ, we need to eliminate $\boldsymbol{\omega}_1$ from (3.1), (3.2). Multiplying both sides of (3.1) by $\boldsymbol{C}_0 \boldsymbol{B}_0^{-1}$ we obtain

$$\boldsymbol{C}_0 \boldsymbol{B}_0^{-1} \boldsymbol{A}_1 \boldsymbol{\omega}_1 = -\boldsymbol{C}_0 \boldsymbol{B}_0^{-1} (\boldsymbol{A}_0 \boldsymbol{\omega}_0 + \boldsymbol{f}_0), \tag{3.4}$$

because (3.2) and (3.3) imply

$$\gamma \boldsymbol{C}_0 \boldsymbol{B}_0^{-1} \boldsymbol{\omega}_0 = -\gamma \boldsymbol{C}_0 \boldsymbol{\psi}_0 = 0. \tag{3.5}$$

Now, $\boldsymbol{\omega}_1$ can be expressed in terms of $\boldsymbol{\omega}_0$ and $\boldsymbol{f}_0$ by solving (3.4) that substituted back into (3.1) results in

$$\gamma \boldsymbol{\omega}_0 = \boldsymbol{D}_0 (\boldsymbol{A}_0 \boldsymbol{\omega}_0 + \boldsymbol{f}_0),$$

where $\boldsymbol{D}_0 = \boldsymbol{I} - \boldsymbol{A}_1 (\boldsymbol{C}_0 \boldsymbol{B}_0^{-1} \boldsymbol{A}_1)^{-1} \boldsymbol{C}_0 \boldsymbol{B}_0^{-1}$ and $\boldsymbol{I}$ is the identity matrix. Note that $\boldsymbol{f}_0$ is linear in both $\boldsymbol{\psi}_0$ and $\boldsymbol{\phi}_0$ where the latter can be expressed as $\boldsymbol{\phi}_0 = \boldsymbol{E}_0^{-1} \boldsymbol{\omega}_{0,y}$ by solving the matrix counterpart of (2.11). Eventually, using (3.2), we can write $\boldsymbol{f}_0 = \boldsymbol{F}_0 \boldsymbol{\psi}_0$, which leads to

$$\gamma \boldsymbol{\psi}_0 = \boldsymbol{B}_0^{-1} \boldsymbol{D}_0 (\boldsymbol{A}_0 \boldsymbol{B}_0 - \boldsymbol{F}_0) \boldsymbol{\psi}_0. \tag{3.6}$$

This complex matrix eigenvalue problem is solved by the LAPACK's ZGEEV routine.

https://doi.org/10.1017/S0022112009993259 Published online by Cambridge University Press

$N_x \times N_y$	c	$N_x \times N_y$	c
20×20	$(0.9515252, -0.02267611)$	20×35	$(0.23219007, -0.3204544 \times 10^{-3})$
24×24	$(0.9514767, -0.02258387)$	25×40	$(0.23237696, -0.5640044 \times 10^{-4})$
28×28	$(0.9514760, -0.02258432)$	30×45	$(0.23239397, -0.28703331 \times 10^{-4})$
32×32	$(0.9514760, -0.02258432)$	30×50	$(0.23239343, -0.21204144 \times 10^{-4})$
36×36	$(0.9514760, -0.02258432)$	40×60	$(0.23239274, -0.21981102 \times 10^{-4})$

TABLE 2. Convergence of the complex relative phase velocity $c = \mathrm{i}\gamma/(Re\,k)$ of the least stable mode of symmetry I for a model base flow $\bar{w}(x, y) = (1 - x^2)(A^2 - y^2)$ with $A = 1$, $Re = 10^4$ and $k = 1$ (left) and for the non-magnetic duct flow with $A = 5$, $Re = 1.04 \times 10^4$ and $k = 0.91$ considered by Tatsumi & Yoshimura (1990) (right).

Without the base flow ($Re = 0$), the leading eigenvalues of (3.6) are real and negative except for $N_x + N_y$ eigenvalues which are zero within machine accuracy. These spurious eigenvalues are caused by the way the boundary condition (3.3) is imposed using (3.5) which can also be satisfied by $\gamma = 0$. These zero eigenvalues can easily be identified and discarded. Alternatively, they can be shifted down the spectrum by an arbitrary value γ_0 when $\gamma_0 \boldsymbol{C}_0 \boldsymbol{\psi}_0$ is added to the right-hand side of (3.4). Note that this transformation does not affect the true eigenmodes which satisfy the boundary condition (3.3). However, our approach is not completely free of unstable spurious eigenmodes which may appear at sufficiently high Re depending on the collocation approximation of inertial terms (2.12), (2.13). Because the collocation differentiation satisfy the product rule approximately rather than exactly (Fornberg 1996), the discretization of inertial terms is affected by the form in which they are presented. We find that the number of unstable spurious eigenmodes is the least when the inertial terms are approximated in the 'conservative' form given by (2.12), (2.13). In contrast to the true eigenmodes, the spurious ones are numerical artifacts which depend strongly on the number of collocation points. This allows us to identify them easily by recalculating the spectrum with $N_x + 1$ and $N_y + 1$ collocation points and retaining only those eigenvalues whose modulus of the relative variation is typically less than $\varepsilon = 10^{-3}$–10^{-4}, which is subsequently referred to as the relative accuracy threshold. Once a true eigenvalue is identified, it can be tracked further by its imaginary part without recalculating the spectrum as the control parameters are slowly varied.

The numerical method has been validated using a model base flow $\bar{w}(x, y) = (1 - x^2)(A^2 - y^2)$ with $A = 1$ at $Re = 10^4$ and $k = 1$ as well as the non-magnetic duct flow with $A = 5$, $Re = 1.04 \times 10^5$ and $k = 0.91$ considered by Tatsumi & Yoshimura (1990) that resulted in the complex relative phase velocity $c = \mathrm{i}\gamma/(Rek)$ for the least stable mode of symmetry I (o, o) which is shown in table 2 for various resolutions. For the model flow, the increase of the resolution from 20×20 to 28×28 collocation points results in the fast convergence of the leading eigenvalue with the accuracy raising from two to seven figures, respectively, which is comparable to the accuracy of the Galerkin method for this test problem used by Uhlmann (2004). Similarly, fast convergence is obvious also for the non-magnetic duct flow with aspect ratio $A = 5$. Owing to the large aspect ratio $A = 5$ as well as the high Reynolds number $Re = 1.04 \times 10^4$, which for $k = 0.91$ is close to its critical value, at least 30×45 collocation points are required to obtain the phase velocity with five accurate figures, which again is comparable to the accuracy of the Galerkin method tested against the same case by Uhlmann & Nagata (2006). Also the instability threshold parameters for the aspect

https://doi.org/10.1017/S0022112009993259 Published online by Cambridge University Press

A	$Re_c \times 10^{-4}$	k_c	c_c
5	1.043	0.9085	0.2321
4	1.819	0.8139	0.2042
3.5	3.650	0.7075	0.1738

TABLE 3. The critical Reynolds number Re_c, wavenumber k_c and phase velocity c_c obtained with 30×50 collocation points for the instability mode I in the non-magnetic duct flow at various aspect ratios A.

$N_x \times N_y$	c $(Ha = 10)$	$N_x \times N_y$	c $(Ha = 10^2)$
20×20	$(0.7579394, -0.3312792 \times 10^{-3})$	25×25	$(0.4907420, -0.8028854 \times 10^{-2})$
25×25	$(0.7579419, -0.3334821 \times 10^{-3})$	30×30	$(0.4907416, -0.8028572 \times 10^{-2})$
30×30	$(0.7579419, -0.3337441 \times 10^{-3})$	35×35	$(0.4907415, -0.8028551 \times 10^{-2})$
35×35	$(0.7579413, -0.3337346 \times 10^{-3})$	40×40	$(0.4907415, -0.8028549 \times 10^{-2})$
40×40	$(0.7579413, -0.3337034 \times 10^{-3})$	45×45	$(0.4907415, -0.8028549 \times 10^{-2})$

$N_x \times N_y$	c $(Ha = 10^3)$
40×40	$(0.5053194, 0.1453188 \times 10^{-2})$
45×45	$(0.5054035, 0.1421803 \times 10^{-2})$
50×50	$(0.5053892, 0.1416928 \times 10^{-2})$
55×55	$(0.5053904, 0.1416891 \times 10^{-2})$
60×60	$(0.5053902, 0.1417051 \times 10^{-2})$

TABLE 4. Convergence of the complex relative phase velocity $c = i\gamma/(Re\,k)$ of the least stable mode for the Hunt's flow in square duct at three different Hartmann numbers: 1) $Ha = 10$, $Re = 2000$, $k = 0.8$, mode II; 2) $Ha = 10^2$, $Re = 10^3$, $k = 5$, mode I; 3) $Ha = 10^3$, $Re = 3 \times 10^3$, $k = 16$, mode I.

ratios $A = 5, 4, 3.5$, which are shown in table 3 for 30×50 resolution, agree well with Tatsumi & Yoshimura (1990).

As seen in table 4, a comparably fast convergence holds also for the complex phase velocity of the least stable modes in the Hunt's flow at $Ha = 10, 10^2, 10^3$. Detailed numerical results for these instability modes are presented in the next section. A typical spectrum of the complex relative phase velocities c is shown in figure 3 for $Ha = 100$ close to the instability threshold for the least stable modes of type I and III. The eigenvalues have been computed using 50×50 collocation points and the relative accuracy threshold $\varepsilon = 10^{-3}$.

Subsequently, to verify the numerical accuracy of the obtained results we recalculate them with the resolution increased by 5 collocation points in each direction. Only the results coinciding by at least four leading figures are retained. For modes I and III, the resolution of 35×35 ensures the accuracy of at least 5 digits at $Ha = 100$, while 50×50 resolution is required at $Ha = 3 \times 10^3$. Modes II and IV require only 30×30 resolution at $Ha \approx 10$, whereas 55×55 points are required at $Ha \approx 400$.

4. Results and discussion

Here we present the results for the flow in a square duct which according to Tatsumi & Yoshimura (1990) is linearly stable in the non-magnetic case. First, we find the base flow numerically and normalize it with respect to its maximum velocity

https://doi.org/10.1017/S0022112009993259 Published online by Cambridge University Press

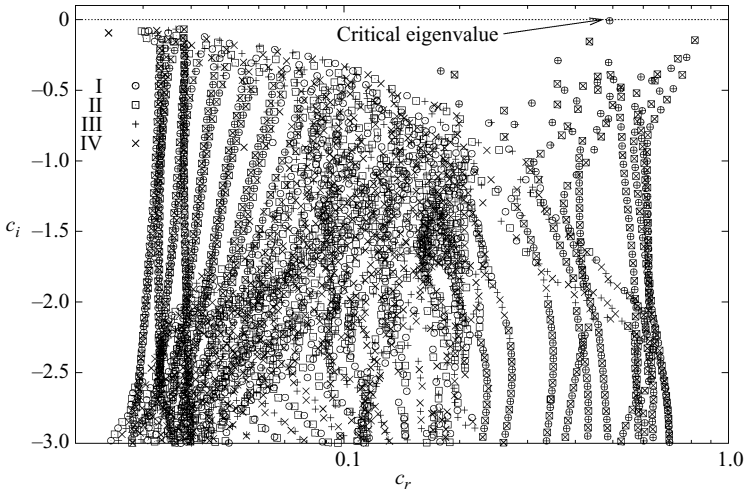


FIGURE 3. Spectrum of the complex relative phase velocities $c = \mathrm{i}\gamma/(Re\,k)$ for all four mode types at $Ha = 100$, $Re = 10^3$, $k = 5$ obtained with 50×50 collocation points and the relative accuracy threshold $\varepsilon = 10^{-3}$.

which is used here as the velocity scale. The flow rate over one quarter of the duct, which is also the average velocity, is found to vary for $Ha \gg 1$ as

$$Q \approx 1.23 Ha^{-1/2} + 3.87 Ha^{-1}, \tag{4.1}$$

where both coefficients are obtained by the best fit of the numerical solution. The main contribution to the flow rate is due to the side jets whereas the next-order correction is due to the core flow. Although the characteristic velocity of the core flow is only $O(Ha^{-1})$ with respect to that of the side layers, its relative contribution to the flow rate is $Ha^{1/2}$ times larger because the relative thickness of side jets is $O(Ha^{-1/2})$. If the flow rate were used for the characteristic velocity, the relative contribution of the core flow in the critical Reynolds number would be $O(Ha^{-1/2})$. In contrast, when the maximum velocity is used for this purpose, the correction is only $O(Ha^{-1})$ which becomes negligible at a much lower Ha than the previous one. This results in a more definite asymptotics appearing at numerically attainable values of Ha. Note that for $Ha = 10^3$ the relative contribution of the core flow to the flow rate is about 10 %. Therefore, we have chosen the maximum rather than average velocity as the characteristic scale.

The neutral stability curves for the instability type II plotted in figure 4 show the marginal Reynolds number, which yields zero growth rate ($\Re[\gamma] = 0$) of the most unstable mode for the given wavenumber, and the relative phase velocity $c = -\omega/(Re\,k)$ at various Hartmann numbers. Here $\omega = \Im[\gamma]$ is the frequency of the corresponding neutrally stable mode. The minimum of the marginal Reynolds number and the corresponding wavenumber at which it occurs give, respectively, the critical value Re_c and the critical wavenumber k_c. This wavenumber along with the corresponding phase velocity is plotted in figure 5 against the Hartmann number. It is seen in figure 5(a) that the mode of type II, which is the most unstable up to $Ha \approx 40$, first appears at $Ha \approx 5.7$. At this Hartmann number, the velocity profile of the base flow, which is very close to those shown in figures 1(b) and 1(c) for $Ha = 6$, has a minimum at the centre of the duct accompanied by two slight maxima at the each side of it. With the increase of the magnetic field, these velocity maxima develop

https://doi.org/10.1017/S0022112009993259 Published online by Cambridge University Press

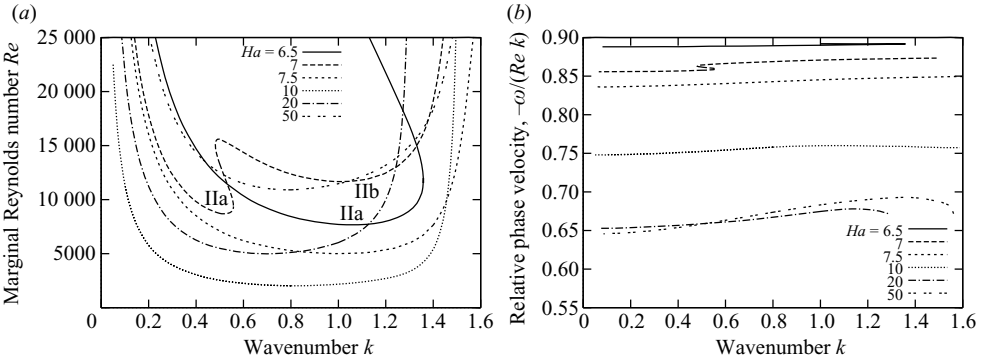


FIGURE 4. Marginal Reynolds number (a) and relative phase velocity (b) versus the wavenumber for neutrally stable modes of type II.

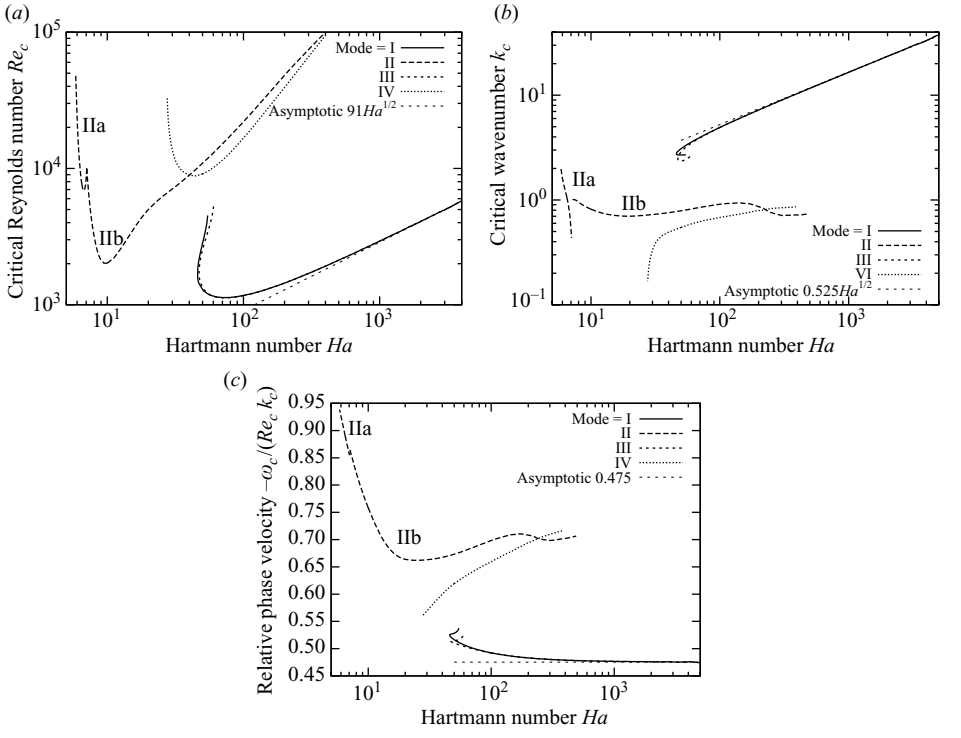


FIGURE 5. Critical Reynolds number (a), wavenumber (b) and relative phase velocity (c) against Hartmann number.

into the jets localized at the sidewalls of the duct (see figure 1c). There are inflection points in the velocity profile, which imply a possibility of an inviscid-type instability, however this criterion is generally restricted to one-dimensional inviscid flows (Bayly, Orszag & Herbert 1988).

Note that in a certain range of the Hartmann number there may be two local minima on the neutral stability curve. These are denoted as (IIa) and (IIb) in figure 4(a). The first minimum, IIa, is below the second one up to $Ha \approx 7$ where the critical mode switches to IIb. The corresponding branches of the critical parameters

https://doi.org/10.1017/S0022112009993259 Published online by Cambridge University Press

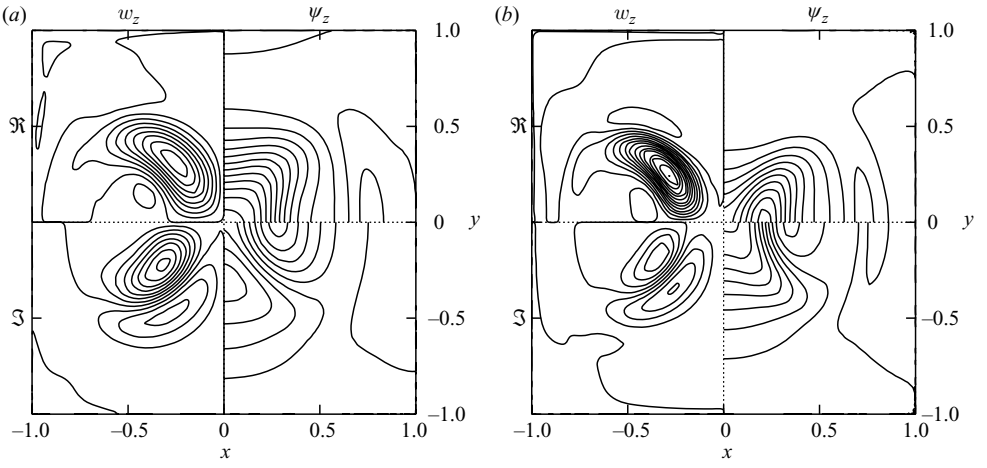


FIGURE 6. Amplitude distributions of real ($y > 0$) and imaginary ($y < 0$) parts of $\hat{w}$ ($x < 0$) and $\hat{\psi}_z$ ($x > 0$) of the critical perturbations over one quadrant of duct cross-section for instability modes IIa (a) and IIb (b) at $Ha \approx 7$ and $Re \approx 10^4$.

for this mode are labelled as IIa and IIb in figure 5. With the increase of Ha, Re_c first steeply decreases down to its minimal value of $Re_c \approx 2018$ at $Ha \approx 10$ and then starts to increase with the rate becoming nearly proportional to Ha for $Ha \gtrsim 40$. It is important to note that the relative phase velocity of the neutrally stable modes, shown in figure 4(b), is nearly invariant with wavenumber, and has the order of magnitude $O(1)$. Moreover, the relative phase velocity is seen in figure 5(c) to stay about $O(1)$ at large Ha as well. Both of these facts imply that the phase velocity of unstable modes is strongly correlated with the maximum velocity defined by Re.

In order to visualize the three-dimensional velocity field of the critical perturbation given by $\Re[\hat{\boldsymbol{v}}(x, y)\mathrm{e}^{\mathrm{i}k_c z}]$ we consider the complex amplitude of the velocity perturbation $\hat{\boldsymbol{v}} = \nabla_k \times \hat{\boldsymbol{\psi}}$ which is associated with the corresponding vector stream function $\hat{\boldsymbol{\psi}}$. The velocity field $(\hat{u}, \hat{v})$ in the (x, y) plane can be decomposed into solenoidal $\hat{\boldsymbol{v}}_s$ and potential $\hat{\boldsymbol{v}}_p$ components which satisfy $\nabla \cdot \hat{\boldsymbol{v}}_s = 0$ and $\nabla \times \hat{\boldsymbol{v}}_p = 0$, respectively. The solenoidal component satisfying the impermeability boundary condition is given by $\hat{\boldsymbol{v}}_s = -\boldsymbol{e}_z \times \nabla \hat{\psi}_z$ which implies that $\hat{\psi}_z$ is the stream function of $\hat{\boldsymbol{v}}_s$. The incompressibility constraint of the whole velocity perturbation, which may be written as $\nabla \cdot \hat{\boldsymbol{v}}_p = -\mathrm{i}k\hat{w}$, in turn, links the potential component $\hat{\boldsymbol{v}}_p$ to the longitudinal velocity perturbation $\hat{w}$, which serves as a source or a sink for the former. Therefore, the whole velocity perturbation is completely defined by $\hat{\psi}_z$ and $\hat{w}$. In a similar way, the streamlines of solenoidal flow components in the (x, z) and (y, z) planes are given by $\hat{\psi}_y$ and $\hat{\psi}_x$, respectively. Note that the perturbation amplitudes are complex quantities whose real and imaginary parts correspond to the instantaneous distributions in the (x, y) plane shifted in time or in space by a quarter of a period.

Distributions of the most unstable perturbation amplitudes of types IIa and IIb are plotted in figure 6 for $Ha \approx 7$ over different quadrants of the duct cross-section. Both perturbations differ mainly by the critical wavenumbers, $k_c \approx 0.44$ and $k_c \approx 1$, respectively, but have similar amplitude distributions concentrated about the centre of the duct. Transversal circulation in the (x, y) plane, which is given by the isolines of $\hat{\psi}_z$, takes place about the centre of the duct with $\hat{v}_x$ and $\hat{v}_y$ being even functions of x and y, respectively. The longitudinal velocity perturbation $\hat{w}$, caused by the advection

https://doi.org/10.1017/S0022112009993259 Published online by Cambridge University Press

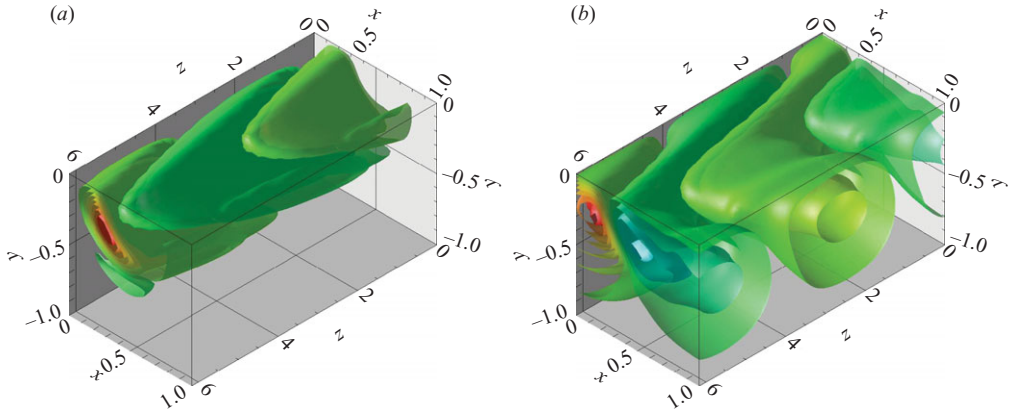


FIGURE 7. Isosurfaces of longitudinal velocity $\hat{w}$ (a) and electric potential $\hat{\phi}$ (b) perturbation over a wavelength in one quadrant of duct cross-section for instability mode IIb at $Ha \approx 7$ and $Re \approx 10^4$.

of momentum of the base flow by the transversal circulation, is an odd function of both x and y. Both of these instability modes are obviously related to the two local velocity maxima which appear first in the centre of the base flow at $Ha \approx 6$. With the increase of Ha these two velocity maxima develop into a pair of jets along the insulating sidewalls (see figure 1b, $x < 0$).

Besides spatial amplitude distributions, the perturbations can be characterized by the kinetic energy distribution over the velocity or vorticity/stream function components as follows:

$$E \propto \int_S |\hat{\boldsymbol{v}}|^2 \, \mathrm{d}s = \int_S \Re[\hat{\boldsymbol{\omega}} \cdot \hat{\boldsymbol{\psi}}^*] \, \mathrm{d}s,$$

where E is the kinetic energy of perturbation averaged over the wavelength. The integrals in the expression above are taken over the duct cross-section S, and the asterisk denotes the complex conjugate. We find that 98 % and 91 % of kinetic energy for modes IIa and IIb, respectively, are carried by the longitudinal velocity perturbation $\hat{w}$. The corresponding component of the vorticity perturbation $(\hat{\omega}_z, \hat{\psi}_z)$, which is associated with the circulation in the (x, y) plane, contains only 2 % and 7 % of kinetic energy, respectively. The isosurfaces of the critical perturbations of longitudinal velocity and electric potential are shown in figure 7 for one wavelength of mode IIb in the right bottom quadrant of duct at $Ha = 7$ and $Re = 10^4$. The corresponding perturbation pattern for mode IIa differs mainly by a longer wavelength. As seen in figure 7(a), the perturbation of $\hat{w}$ represents a pair of elongated, slightly tilted and periodically overlapping streaks located close to the centre of the duct. The perturbation of the electric potential, which is the largest in the vertical mid-plane of the duct ($x = 0$), partly reaches the sidewalls where it can be measured experimentally.

Neutral stability curves for the instability mode of type IV, which appears for $Ha \gtrsim 28$ and differs from the previous one by the opposite x parity, are plotted in figure 8. Figure 5 shows that Re_c of this mode, which for low values of Ha lies above that of mode II, first steeply decreases with Ha by reaching $Re_c \approx 9 \times 10^3$ of mode II at $Ha \approx 40$. The critical Reynolds number for mode IV attains a minimum of

https://doi.org/10.1017/S0022112009993259 Published online by Cambridge University Press

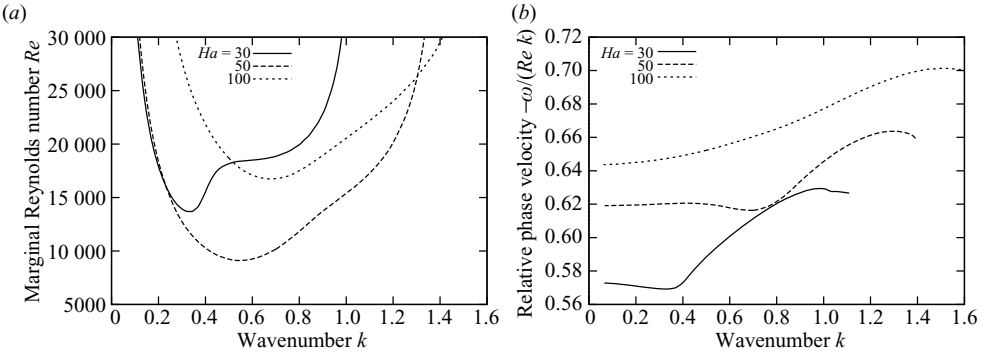


FIGURE 8. Marginal Reynolds number (a) and relative phase velocity (b) versus the wavenumber for neutrally stable modes of type IV.

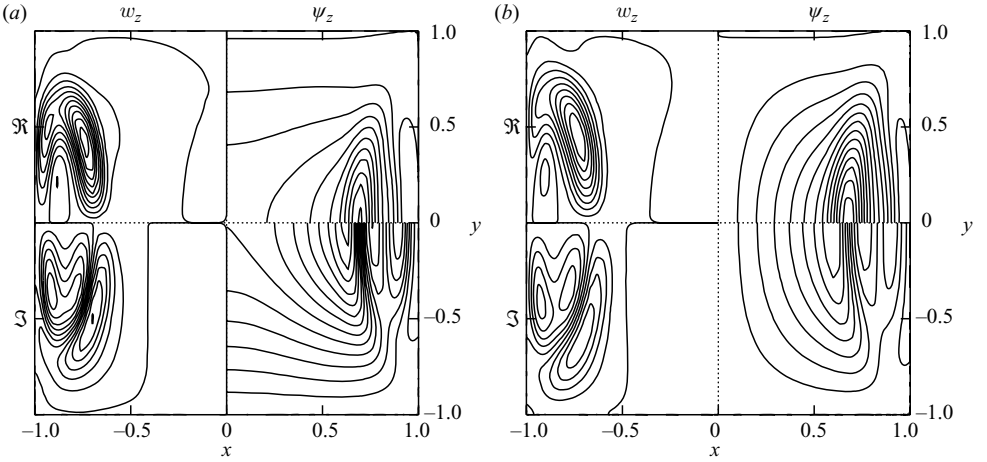


FIGURE 9. Amplitude distributions of real ($y > 0$) and imaginary ($y < 0$) parts of $\hat{w}$ ($x < 0$) and $\hat{\psi}_z$ ($x > 0$) of the critical perturbations over one quadrant of duct cross-section for instability modes II (a) and IV (b) at $Ha \approx 40$ and $Re \approx 9 \times 10^4$.

$Re_c \approx 8.8 \times 10^3$ at $Ha \approx 44$ and then starts to increase with Ha remaining below Re_c for mode II up to the largest numerically attainable value of $Ha \approx 400$.

Amplitude distributions of the most unstable perturbations of types II and IV are plotted in figure 9 at $Ha \approx 40$ and $Re \approx 9 \times 10^3$. The critical wavenumbers for these modes are, respectively, $k_c \approx 0.75$ and $k_c \approx 0.49$. It is seen in figure 9(a) that mode II has moved from the centre of duct, where it originally appeared at $Ha \approx 5.7$, to the sidewall. The only principal difference between these modes is the opposite x parity which results in a pair of mirror-symmetric longitudinal vortices on each side of the duct with the same or opposite sense of circulation for modes II and IV, respectively. In the first case, both vortices are partly connected across the vertical mid-plane of the duct whereas they are separated by that plane in the second case. For both modes, the perturbations of the longitudinal velocity are localized in the sidewall jets and are very similar to each other except for the opposite phases of oscillations across the width of the duct. Modes II and IV are also similar from the energetic point of view with 88 % and 93 % of kinetic energy concentrated in the perturbation of the longitudinal velocity. The least amount of energy, which is about 1 % and 0.4 %,

https://doi.org/10.1017/S0022112009993259 Published online by Cambridge University Press

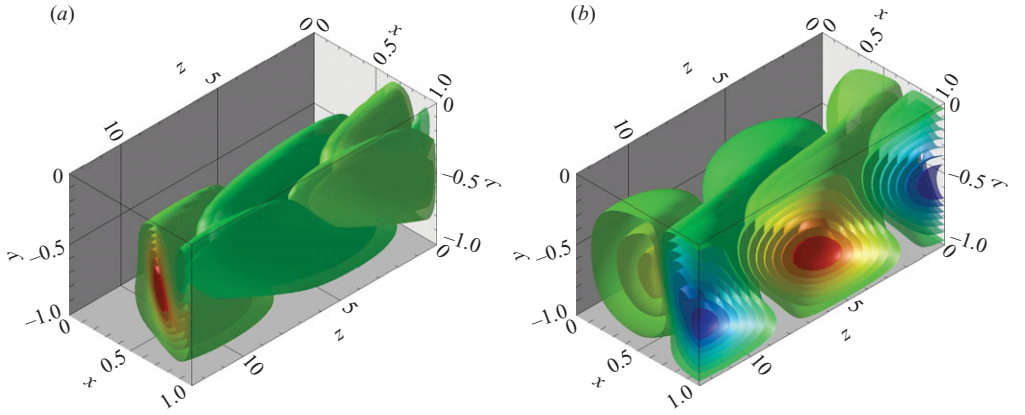


FIGURE 10. Isosurfaces of longitudinal velocity w (a) and electric potential ϕ (b) perturbation over a wavelength in one quadrant of duct cross-section for instability mode IV at $Ha \approx 40$ and $Re \approx 9 \times 10^4$.

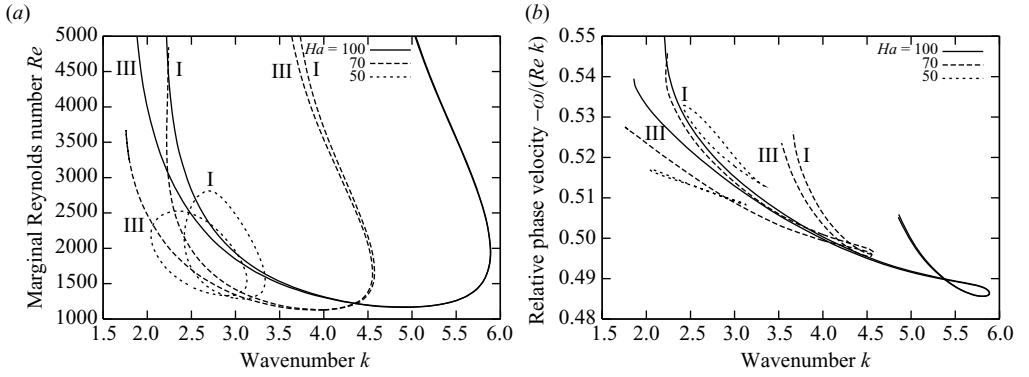


FIGURE 11. Marginal Reynolds number (a) and relative phase velocity (b) versus the wavenumber for neutrally stable modes of types I and III.

respectively, is contained in the x component of the velocity perturbation while the rest is carried by the y component parallel to the magnetic field.

The isosurfaces of the critical perturbations of the longitudinal velocity and of the electric potential for mode IV are shown in figure 10 over one wavelength in the right bottom quadrant of duct for $Ha = 40$ and $Re \approx 9 \times 10^3$. In this case, the distributions of $\hat{w}$ and $\hat{\phi}$ are even and odd functions of x, respectively. The corresponding pattern for mode II at these parameters differs from that of mode IV mainly by the shorter wavelength and opposite x parity that results in a non-zero perturbation of $\hat{\phi}$ in the vertical mid-plane of the duct ($x = 0$).

A pair of additional instability modes of type I and III appears for $Ha \gtrsim 46$ and 47, respectively. These modes differ from the ones of type II and IV by the opposite y parity. The neutral stability curves plotted in figure 11 look very similar for both of these modes. First, for $Ha \lesssim 54$, 60 the neutral stability curves are seen to form closed loops which implies that both modes are unstable only within limited ranges of Reynolds and wavenumbers. In this range of Ha, there is not only the lower but also the upper critical value of Re, by exceeding which all perturbations of the corresponding type become linearly stable again.

https://doi.org/10.1017/S0022112009993259 Published online by Cambridge University Press

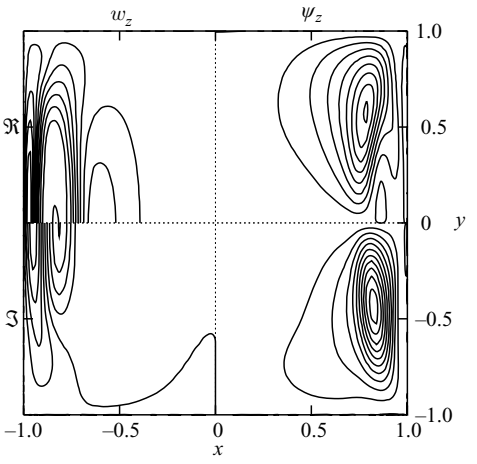


FIGURE 12. Amplitude distributions of real ($y > 0$) and imaginary ($y < 0$) parts of $\hat{w}$ ($x < 0$) and $\hat{\psi}_z$ ($x > 0$) of the critical perturbations over one quadrant of duct cross-section for instability mode I at $Ha \approx 100$ and $Re_c \approx 1170$.

These critical values of Re, which are considerably lower than those for the previous two modes, are plotted in figure 5 against the Hartmann number along with the corresponding wavenumbers and the relative phase velocities. As seen in figure 5(a), the upper critical Reynolds number steeply increases with Ha, becoming very large at $Ha \approx 54$, 60 for modes I and III, respectively. The lower value of Re_c steeply decreases to its minimum $Re_c \approx 1130$ attained at $Ha \approx 70$. A further increase of Ha results in the growth of the critical Reynolds number for both modes approaching the asymptotics $Re_c \approx 91 Ha^{1/2}$ for $Ha \gg 1$. This implies that the critical Reynolds number based on the average velocity tends to a constant $\bar{R}e_c \approx 112$ while the next-order correction is about $352 Ha^{-1/2}$. In contrast to this, the relative next-order correction for Re_c based on the maximal velocity, as discussed at the beginning of this section, is only $O(Ha^{-1})$. The critical wavenumber for both modes I and II tends to $k_c \approx 0.525 Ha^{1/2}$. This means that the critical wavelength reduces directly with the characteristic thickness of the parallel layers $O(Ha^{-1/2})$. The relative phase velocity for both modes is seen to tend asymptotically to a constant $c_c \approx 0.475$ which confirms that this instability is indeed associated with the sidewall jets and, thus, it is completely determined by the characteristic thickness and by the velocity of those jets. Note that the relative phase velocity of two other modes of type II and IV is also $O(1)$ which implies that these instabilities are associated with the sidewall jets, too. However, the critical wavenumber for modes II and IV remains $O(1)$ even for $Ha \gg 1$. This, in turn, implies that both of these instability modes are caused by the velocity variation over the height rather than the thickness of the jet. Thus, the height rather than thickness of the jet serves as the characteristic length scale for modes II and IV.

Figure 12 shows the amplitude distribution of the most unstable perturbation for type I only because it is almost identical to that for type III except for the opposite y parity. In this case, however, the y parity has almost no effect on the amplitude distributions on each side of the duct because perturbations are localized in the jets at the sidewalls and practically do not interact with each other. As it is seen, for both modes of type I and III, the component of velocity perturbation along the magnetic

https://doi.org/10.1017/S0022112009993259 Published online by Cambridge University Press

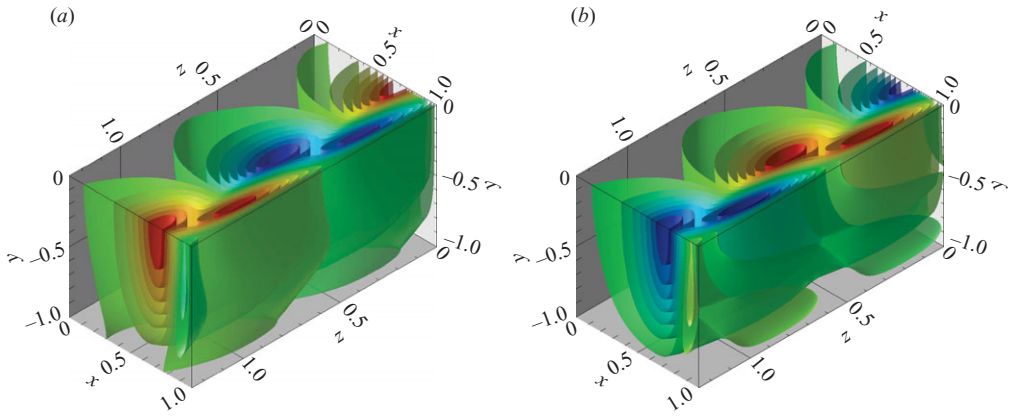


FIGURE 13. Isosurfaces of ψ_y (a) and electric potential ϕ (b) perturbation over a wavelength in one quadrant of duct cross-section for instability mode I at $Ha \approx 100$ and $Re \approx 1170$.

field is an odd function of y whereas the other two velocity components are even functions. Thus, the transversal circulation in the (x, y) plane involves a couple of vertically mirror-symmetric vortices at each sidewall, while the perturbation of the longitudinal velocity w, which is an even function of y, is rather uniform along the magnetic field in the horizontal mid-part of the duct.

From the energetic point of view, it turns out that 70 % and 23 % of the kinetic energy are carried by the z and x components of the velocity perturbation, while only 7 % are carried by the y component. Thus, 89 % of kinetic energy is concentrated in the y component of vorticity/stream function perturbation, which is associated with the z and x velocity components. The x and z components of vorticity/stream function associated with the y component of velocity contain only 6 % and 5 % of the energy. Consequently, in this case, the perturbation of the flow is well represented by ψ_y alone whose isosurfaces, plotted in figure 13(a) for mode I, show the isolines of solenoidal circulation in the horizontal plane. The corresponding isosurfaces of the electric potential perturbation are shown in figure 13(b).

5. Summary and conclusions

In this study we have analysed numerically the linear stability of the flow of a liquid metal in a square duct subject to a transverse magnetic field. The walls of the duct perpendicular and parallel to the magnetic field are perfectly conducting and insulating, respectively. We used a novel three-dimensional vector stream function formulation and Chebyshev collocation method to solve the eigenvalue problem for small-amplitude perturbations. Due to the two-fold reflection symmetry of the base flow with respect to the $x = 0$ and $y = 0$ planes the perturbations with four different parity combinations over the duct cross-section decouple from each other.

The base flow, which without the magnetic field is linearly stable in a square duct, becomes unstable at the Hartmann number $Ha \approx 5.7$ as two velocity maxima in the centre of the duct appear. This instability mode, which is the most dangerous at low Hartmann numbers, involves the vorticity component in the direction of the magnetic field which is antisymmetric and, thus, essentially non-uniform along the field and symmetric in the spanwise direction across the duct. The velocity component

https://doi.org/10.1017/S0022112009993259 Published online by Cambridge University Press

in the direction of the magnetic field for this mode is symmetric along the field and antisymmetric in the spanwise direction, respectively. This mode becomes the most unstable at $Ha \approx 10$ where its critical Reynolds number based on the maximal velocity attains a minimum of $Re_c \approx 2018$. The increase of the magnetic field results in the stabilization of this mode with Re_c growing approximately as Ha. For $Ha \gtrsim 40$ another mode with the opposite spanwise parity across the duct becomes the most dangerous and remains such up to $Ha \approx 46$. These two instability modes have most of their kinetic energy concentrated in long streak-like perturbations of the streamwise velocity which first appear close to the centre of the duct and then move to the sidewall layers as the magnetic field increases. The critical wavenumber is $O(1)$ that corresponds to the critical wavelength considerably exceeding the width of the duct. It is important to note that the critical phase velocity remains $O(1)$ even in a relatively strong magnetic field. This implies that for $Ha \gg 1$ both of these instability modes are associated with the sidewall jets.

At $Ha \approx 46$ a pair of two additional instability modes appears with the parity along the magnetic field being opposite to that of the previous two modes. The critical Reynolds number, which is very close for both modes, attains a minimum of $Re_c \approx 1130$ at $Ha \approx 70$ and increases as $Re_c \approx 91 Ha^{1/2}$ for $Ha \gg 1$. The corresponding critical wavelength is $k_c \approx 0.525 Ha^{1/2}$ while the critical phase velocity approaches 0.475 of the maximum jet velocity. This again suggests these two instability modes, similarly to the first two, to be associated with the side jets. The main difference between the first and second pairs of disturbances is in their critical wavenumbers which are $O(1)$ and $O(Ha^{1/2})$, respectively. The latter means that the critical wavelength scales directly with the side layer thickness $O(Ha^{-1/2})$, which serves as the characteristic length scale for the last two instability modes. The critical wavenumber of the first two instability modes being $O(1)$ implies that they are associated with the velocity variation over the height of the parallel layer whereas the last two modes are associated with the velocity variation over the thickness of this layer. From the energetic point of view, the last two instability modes have most of their kinetic energy concentrated in the vortical flow component along the magnetic field which corresponds to the fluid circulation in the planes transverse to the field.

These last two modes are analogous to the side-layer instability mode found by Ting *et al.* (1991) for the flow in the duct with thin but relatively well-conducting walls for $Ha \gg 1$. The critical Reynolds number based on the average velocity for the latter is $\bar{R}e_c \approx 313$ compared to our result $\bar{R}e_c \approx 112$ which is rescaled by the average velocity (4.1). On the other hand, our $\bar{R}e_c$ is several times higher than the corresponding result of Fujimura (1989) for the two-dimensional approximation. Note that this approximation incorrectly predicts the base flow in a square duct to remain linearly unstable in the limit of vanishing magnetic field strength whereas a significant destabilization is predicted at the Hartmann numbers as small as $Ha \approx 10$. In addition, note that the instability predicted at $Ha \approx 10$ by our analysis is essentially three-dimensional, as discussed above, and, thus, it is principally different from the two-dimensional one found by Fujimura (1989). Further comparison with the results of Ting *et al.* (1991) shows that our critical wavenumber $\bar{k}_c \approx 0.525$ scaled by the side-layer thickness $Ha^{-1/2}$ is close to their asymptotic value $k_{cr} = 0.55$. At the same time, their phase velocity $c_c = 0.0947$ appears to be significantly lower than ours $\bar{c}_c = 0.423$, when rescaled with respect to the average velocity. Moreover, the instantaneous streamlines in the horizontal mid-plane for the critical perturbation plotted in figure 13(*a*) show disconnected subvortices at the sidewall whereas those of Ting *et al.* (1991) although being similarly deformed are fully connected single

https://doi.org/10.1017/S0022112009993259 Published online by Cambridge University Press

vortices. These differences may be due to the different physical model used by Ting *et al.* (1991) as discussed in the Introduction.

In conclusion, note that transiently growing small-amplitude perturbations may appear below the linear stability threshold due to the so-called non-normality of the linearized operator (Trefethen *et al.* 1993). Transient growth is sought to account for the bypass transition to turbulence in the shear flows with a high or none at all linear stability threshold (Grossmann 2000). Such a subcritical transition can hardly be relevant for the Hunt's flow in strong magnetic fields ($Ha \gtrsim 50$) because the local critical Reynolds number based on the thickness of side layers is already very low ≈ 100. However, it may still be relevant for weaker magnetic fields, in which the linear stability threshold is much higher or absent at all, when $Ha < 5.7$. But even in the latter case, linear transient growth mechanism might be of limited importance because, as argued by Waleffe (1995), '*... the question of transition is really a question of existence and basin of attraction of nonlinear self-sustaining solutions that have little contact with the nonnormal linear problem*'. For a non-magnetic square duct flow, such nonlinear self-sustaining solutions in the form of finite amplitude travelling waves have been found recently by Wedin, Bottaro & Nagata (2009) and for the magnetic case by Kinet, Knaepen & Molokov (2009).

For a flow in the duct with thin conducting walls, the critical Reynolds numbers observed experimentally by Reed & Picologlou (1989) appear considerably higher than those predicted by the linear stability theory of Ting *et al.* (1991). This may be owing to the fact that the flow in the experiment was developing with jets accelerating which would render them more stable, or that the probes could not reach the thin parallel layer where the instabilities occur first. However, this may also imply that the side-layer instability is supercritical. Then the delay of the transition to turbulence significantly above the linear stability threshold can be accounted for by the distinction between the convective and absolute instabilities. The conventional stability analysis presented in this paper yields the convective instability threshold at which the flow becomes able to amplify certain externally imposed perturbations (Landau & Lifshitz 1987). For a small-amplitude supercritical perturbation in the form of travelling wave to become self-sustained absolute instability is necessary (Lifshitz & Pitaevskii 1981).

The authors are indebted to Leverhulme Trust for financial support of this work and to the Faculty of Engineering and Computing of Coventry University for providing access their high performance computer cluster.

REFERENCES

Bayly, B. J., Orszag, S. & Herbert, T. 1988 Instability mechanisms in shear-flow transitions. *Annu. Rev. Fluid Mech.* **20**, 359–391.

Bühler, L. 2007 Liquid metal magnetohydrodynamics for fusion blankets. In *Magnetohydrodynamics – Historical Evolution and Trends* (ed. S. Molokov, R. Moreau & H. K. Moffatt), pp. 171–194, Springer.

Davidson, P. A. 1995 Magnetic damping of jets and vortices. *J. Fluid Mech.* **299**, 153–186.

Davidson, P. A. 1999 Magnetohydrodynamics in materials processing. *Annu. Rev. Fluid Mech.* **31**, 273–300.

Fornberg, B. 1996 *A Practical Guide to Pseudospectral Methods*. Cambridge University Press.

Fujimura, K. 1989 Stability of MHD flow through a square duct. *UCLA technical report, UCLA–FNT–023*, 27pp.

Gelfgat, Yu. M., Dorofeev, V. S. & Scherbinin, E. V. 1971 Experimental investigation of the velocity structure of an MHD flow in a rectangular channel. *Magnetohydrodynamics* **7**, 26–29.

Grossmann, S. 2000 The onset of shear flow turbulence. *Rev. Mod. Phys.* **72**, 603–618.

https://doi.org/10.1017/S0022112009993259 Published online by Cambridge University Press

Hunt, J. C. R. 1965 Magnetohydrodynamic flow in rectangular ducts, *J. Fluid Mech.* **21**, 577–590.

Jackson, J. D. 1998 *Classical Electrodynamics*. Wiley, § 6.3.

Kakutani, T. 1964 The hydromagnetic stability of the modified plane Couette flow in the presence of a transverse magnetic field. *J. Phys. Soc. Japan* **19**, 1041–1057.

Kinet, M., Knaepen, B. & Molokov, S. 2009 Instabilities and transition in magnetohydrodynamic flows in ducts with electrically conducting walls. *Phys. Rev. Lett.* **103**, 154501.

Landau, L. & Lifshitz, E. M. 1987 *Fluid Mechanics*. Pergamon, § 28.

Lehnert, B. 1952 On the behaviour of an electrically conductive liquid in a magnetic field. *Ark. Fys.* **5,** 69–90.

Lifshitz, E. M. & Pitaevskii, L. P. 1981 *Physical Kinetics*. Pergamon, § 62.

Moffatt, H. K. 1967 On the suppression of turbulence by a uniform magnetic field. *J. Fluid Mech.* **28**, 571–592.

Molokov, S. 1993 Fully developed liquid–metal flow in multiple rectangular ducts in a strong uniform magnetic field. *Eur. J. Mech.* /B *Fluids* **12**, 769–787.

Molokov, S. & Bühler, L. 1994 Liquid–metal flow in a U-bend in a strong uniform magnetic field. *J. Fluid Mech.* **267**, 325–352.

Moreau, R. 1990 *Magnetohydrodynamics*. Kluwer.

Mück, B. 2000 Three dimensional simulation of MHD side–layer instabilities. In *Fourth Intl PAMIR Conf. "Magnetohydrodynamics at Dawn of Third Millennium"*, vol. 1, pp. 297–302. Giens, France.

Platnieks, I. & Freibergs, J. 1972 Turbulence and some problems in the stability of flows with M–shaped velocity profiles. *Magnetohydrodynamics* **8**, 164–168.

Reed, C. B. & Picologlou, B. F. 1989 Sidewall flow instabilities in liquid metal MHD flows under blanket relevant conditions. *Fusion Tech.* **15**, 705–715.

Stieglitz, R., Barleon, L., Bühler, L. & Molokov, S. 1996 Magnetohydrodynamic flow in a right angle bend in a strong magnetic field. *J. Fluid Mech.* **326**, 91–123.

Tatsumi, T. & Yoshimura, T. 1990 Stability of the laminar flow in a rectangular duct. *J. Fluid Mech.* **212**, 437–449.

Ting, A. L., Walker, J. S., Moon, T. J., Reed, C. B. & Picologlou, B. F. 1991 Linear stability analysis for high-velocity boundary layers in liquid–metal magnetohydrodynamic flows. *Intl J. Engng Sci.* **29**, 939–948.

Trefethen, L. N., Trefethen A. E., Reddy, S. C. & Driscoll, T. A. 1993 Hydrodynamic stability without eigenvalues. *Science* **261**, 578–584.

Uhlmann, M. 2004 Linear stability analysis of flow in an internally heated rectangular duct. *Tech. Rep.* 1043, CIEMAT, Madrid, Spain, ISSN 1135–9420.

Uhlmann, M. & Nagata, M. 2006 Linear stability of flow in an internally heated rectangular duct. *J. Fluid Mech.* **551**, 387–404.

Waleffe, F. 1995 Transition in shear flows: nonlinear normality versus non-normal linearity. *Phys. Fluids* **7**, 3060–3066.

Wedin, H., Bottaro, A. & Nagata, M. 2009 Three-dimensional travelling waves in a square duct. *Phys. Rev.* E **79**, 065305–065304.

https://doi.org/10.1017/S0022112009993259 Published online by Cambridge University Press